ADVANCED FUNCTIONAL MATERIALS
www.afm-journal.de

In-Situ Study of Photo-Rechargeable Aqueous Zinc-Ion Batteries with the Bifunctional α-MnO_2 Photoelectrodes

*Zhaobo Zheng, Chenzhi Ding, Md Saif Hasan, Kao Wang, Yue Liu, Wei Yang, Jingzhao Cheng, Zhengtang Luo, Shaowen Cao, and Yao Ding**

Directly harvesting solar power without traditional solar cells represents an efficient solution to the current energy challenges. Photo-rechargeable batteries (PRBs) are receiving intense interest as they eliminate the additional costs and energy losses associated with off-grid power generation. Herein, photo-rechargeable aqueous Zinc-ion batteries (PRZIBs) are constructed, using α-MnO_2 nanowires as bifunctional photoelectrodes to reveal the complex photo-electrochemical effects in MnO_2 PRZIBs. Through a series of in situ characterizations under illumination, the advantages of intrinsic light effects in α-MnO_2 based PRZIBs are elucidated from three aspects: (1) inhibition of Jahn-Teller distortion via strengthened hydrogen bonding within α-MnO_2, (2) suppression of Mn^{2+} dissolution through the "protective layers" formed by photo-promoted Zn^{2+}/H^+ co-intercalation, and (3) acceleration of Zn^{2+} desolvation in the electrolyte enabled by abundant photogenerated holes. The PRZIBs with α-MnO_2 photoelectrodes demonstrate a specific discharge capacity of 308.1 mAh g^{-1} under illumination (1 sun), along with excellent cycling stability and high energy conversion efficiency of 0.68% (by photocharging only). In addition, the interdigital micro-PRZIBs successfully power wearable sensors, demonstrating practical applicability. This work provides valuable insights into the time-resolved reaction mechanisms in PRZIBs, and opens new prospects for developing PRBs in wearable and portable devices, i.e. smart textiles and biosensors.

1. Introduction

The non- renewable nature of conventional energy sources and their associated environmental pollution have prompted a shift toward the development of renewable and clean energy. Solar energy, recognized as a viable alternative, can provide $\approx 3 \times 10^{24}$ J of energy annually to Earth's surface.[1] While solar cells have achieved widespread adoption for energy conversion, off-grid solar systems still requires development. For the off-grid power supplies, an external power source is typically needed for electricity storage due to the intermittent nature of solar energy, along with the need for output voltage matching with the energy storage units. These requirement inevitably lead to the energy transmission losses.[2] Therefore, a photo-driven self-powered energy storage system is particularly important.[3] Recently, photo-rechargeable batteries (PRBs) have been widely studied for their integrated bifunctional photovoltaic electrodes.[4] In PRBs, photo-generated holes and electrons accelerate the redox reactions at the photo-cathodes and anodes, effectively converting solar energy into electrochemical energy with fewer independent energy models.[5] Compared to traditional solar cells and energy storage devices, photo-rechargeable batteries offer advantages of lower cost and less energy loss. These benefits make PRBs ideal candidates for powering portable and wearable smart devices, e.g., biosensors, laptops, and smartwatches. Moreover, PRBs demonstrate great potential for off-grid power generation in various scenarios includes remote areas, islands, and communication base stations.[6]

Since the first Li^+-based PRBs were discovered in 2014,[7] significant efforts have been devoted to researching PRBs due to their simple designs and high solar energy conversion efficiency. To achieve such a system, dual-functional (solar conversion and energy storage) photoactive electrodes are essential for integrating the modules and enhancing the performance of PRBs. However, ideal-functional electrodes face some challenges regarding their efficiency, stability, and compatibility.[8] Efficiency requires strong photoelectrochemical properties of the photoactive electrodes, including fast electron-hole separation and transfer, high visible light absorption, and appropriate energy level

Z. Zheng, C. Ding, K. Wang, Y. Liu, W. Yang, Y. Ding
School of Materials Science and Engineering
Wuhan University of Technology
Wuhan 430070, P. R. China
E-mail: ydingaf@whut.edu.cn
J. Cheng, S. Cao
State Key Laboratory of Advanced Technology for Materials Synthesis and Processing
Wuhan University of Technology
Wuhan 430070, P. R. China
Y. Ding
Hubei Longzhong Laboratory
Xiangyang 441000, P. R. China
M. S. Hasan, Z. Luo
Department of Chemical and Biological Engineering and William Mong Institute of Nano Science and Technology
Hong Kong University of Science and Technology
Clear Water Bay, Kowloon, Hong Kong 999077, P.R. China

The ORCID identification number(s) for the author(s) of this article can be found under https://doi.org/10.1002/adfm.202500182

DOI: 10.1002/adfm.202500182

alignment with the electrochemical reaction. Stability pertains to the structural integrity of photoelectrodes during redox reaction, while compatibility refers to their ability to harmonize with the electrolyte. Guided by these principles, various photoelectrode materials (e.g. perovskites,[9] transition metal chalcogenides,[10] metal oxides,[11] and organic small molecules[12]) have been widely explored in energy storage systems, including lithium-ion batteries (LIBs),[9] lithium-sulfur batteries (Li-S batteries),[13] and Aluminum-ion batteries (AIBs).[14] Nevertheless, these approaches still yield limited solar energy conversion efficiencies and face challenges such as high manufacturing costs and stringent safety concerns.

Recently, aqueous zinc ion batteries (ZIBs) have garnered significant attention as promising energy storage systems for wearable devices due to their inherent safety and low costs.[15] Consequently, photo-rechargeable zinc ion batteries (PRZIBs) are emerging as potential power sources for everyday electronics. To date, photoactive materials such as MoS_2,[10] SnO_2,[16] vanadium oxides (e.g., V_2O_5, VO_2, and V_2O_3)[17] and their composites have been reported as the photoelectrodes of PRZIBs. Notably, Boruah's group pioneered the first PRZIBs with V_2O_5 as a photocathode, leveraging its high reversible capacity (≈375 mAh g^{-1}) and optimal bandgap for light harvesting (≈2.2 eV).[17a] Subsequently, researchers focused on hetero-structured photoelectrodes to improve solar energy conversion efficiency due to their high carrier separation ability. For instance, Xu *et al.* demonstrated a MoS_2/SnO_2 heterostructure as the photocathode of PRZIBs, achieving a specific discharge capacity of 202.5 mAh g^{-1} (0.1 A g^{-1}) and a solar conversion efficiency of 0.4% (under 1-sun illumination) after photocharging.[10] Despite these advances, the synergy between the photovoltaic effect and energy storage mechanism in these PRZIBs remains poorly understood. A critical knowledge gap lies in time-resolved mechanistic studies, such as in situ XRD, in situ TEM, and in situ FT-IR, to elucidate photo-assisted processes during energy conversion and storage, which are still unexplored.

Herein, for the first time, α-MnO_2 nanowires are introduced as photoelectrodes in PRZIBs, leveraging their outstanding photoelectrochemical properties, low cost, non-toxicity, and suitable bandgap, which underscore their potential for commercial applications. UV-vis absorption spectra and cyclic photocurrent measurements verify the α-MnO_2 photoelectrodes' superior visible-light absorption and efficient electrons/holes separation. Moreover, in situ XRD and ex-situ XPS characterizations under illumination further reveal the photo-accelerated Zn^{2+}/H^+ co-intercalation mechanism in α-MnO_2, exhibiting faster kinetics compared to dark conditions. This process enhances hydrogen bonding within α-MnO_2, leading to the formation of a new intermediate product, i.e. $Zn_4SO_4(OH)_6{\cdot}5H_2O$. Importantly, in situ FT-IR analysis reveals that photoenergy strengthens the hydrogen bonds (strong H-bonds) in $ZnSO_4$ electrolyte and reinforces the hydrogen-bonding network in the aqueous solvent (H_2O), thereby lowering the energy barrier for Zn^{2+} desolvation. Furthermore, photoinduced Zn^{2+}/H^+ co-intercalation intensifies the H-bonds in α-MnO_2, mitigating Jahn-Teller distortion and suppressing Mn^{2+} dissolution. The PRZIBs with α-MnO_2 photoelectrodes achieve a specific discharge capacity of 308.1 mAh g^{-1} under illumination (1 sun) – significantly higher than 207.2 mAh g^{-1} observed in dark conditions at 0.2 A g^{-1}– along with stable cycling performance and a high energy conversion efficiency of 0.68% (by photocharging only). Additionally, interdigital micro-PRZIBs based on α-MnO_2 photoelectrodes have been successfully integrated into a self-powered pressure sensor, operating without an external energy supply after photocharging. This work provides valuable insights into the real reaction mechanisms of PRZIBs under illumination and establishes a framework for designing efficient two-electrode photo-rechargeable systems for wearable and portable devices, such as smart textiles and biosensors.

2. Results and Discussion

The α-MnO_2 nanowires are usually synthesized by a modified one-step hydrothermal method[14] (see Methods for details). As shown in **Figure 1a**, X-ray diffraction (XRD) spectroscopy confirms that the as-received MnO_2 matches well with the standard α-MnO_2 (PDF #44-0141), with no detectable impurities, indicating high phase purity. The Raman spectrum (Figure S1, Supporting Information) further corroborates the α-MnO_2 structure, exhibiting characteristic peaks centered at 637 cm^{-1} (Mn-O symmetric vibrations), 579 cm^{-1} (Mn-O stretching vibration), and 379 cm^{-1} (Mn-O bending vibration).[18] Additionally, the transmission electron microscopy (TEM) image (Figure 1b) reveals the 1D structure of the α-MnO_2 nanowire, with an average diameter of 20–30 nm (Figure S2, Supporting Information). The lattice fringe spacing of 0.5 nm corresponds to the (2 0 0) plane of tetragonal α-MnO_2. Furthermore, the corresponding selected-area electron diffraction (SAED) pattern in Figure 1c confirms the single-crystal property of α-MnO_2. At the molecular level, the α-MnO_2 consists of corner-sharing double-chain MnO_6 octahedra with well-defined [2 × 2] channels and [1 × 1] tunnels (Figure 1d).[19] The [2 × 2] channels facilitate Zn^{2+} insertion, whereas the [1 × 1] tunnels facilitate H^+ insertion. Under illumination, photoenergy helps to overcome the desolvation energy barrier for $[Zn(H_2O)_6]^{2+}/H_3O^+$ in the electrolyte, promoting the Zn^+/H^+ intercalation during discharge and enhancing the discharge capacity (detailed discussions presented in the following part).

The conduction band (CB) and valence band (VB) positions of α-MnO_2 were characterized using UV-Vis diffuse reflectance spectroscopy and X-ray photoelectron spectroscopy (XPS). The band gap was determined to be 1.95 eV (Figure 1e), while Figure 1f indicates that the valence band is located at 1.69 eV (vs. NHE). Consequently, the CB and VB of α-MnO_2 were calculated as −4.24 eV and −6.19 eV (vs. vacuum), respectively. Figure 1h illustrates PRZIB's structure employing α-MnO_2/rGO electrodes, along with their band diagram and the ions/electrons transport during photocharging. Under illumination, efficient charge separation occurs in the α-MnO_2/rGO photoelectrodes. Specifically, the α-MnO_2 efficiently absorbs photons to generate electron-hole pairs, the photo-generated electrons migrate from VB toward CB, and then rapidly transport to the rGO. Conversely, the holes react with the product of the discharge process, i.e. $ZnMn_2O_4$ (ZMO), facilitating the Zn^{2+} deintercalation process. To assess the charge separation, coin cells with optical windows were assembled for photo-responsive testing (Figure S3, Supporting Information). Figure 1g demonstrates the remarkable photogenerated

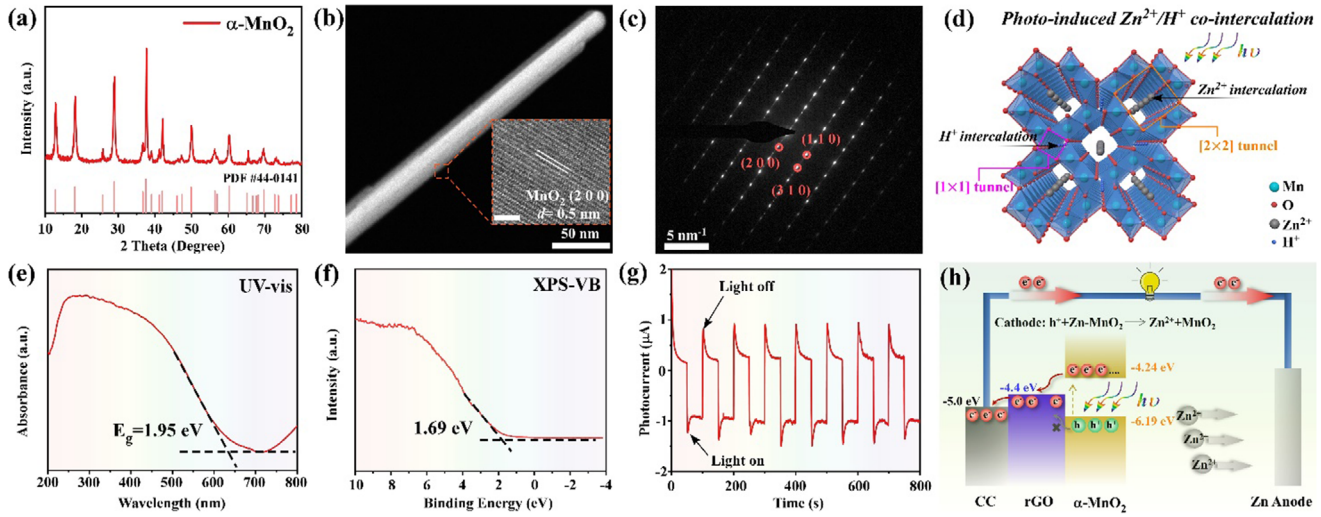

Figure 1. Characterizations and photovoltaic properties of α−MnO_2. a) XRD patterns of α-MnO_2. b) TEM and HRTEM (inset) images of α-MnO_2. Scale bar of inset: 2 nm. c) Corresponding SAED pattern of α-MnO_2. d) Schematic illustration of photo-induced Zn^{2+}/H^+ co-insertion of α-MnO_2 under illumination. e) UV-visible diffuse reflectance spectrum of α-MnO_2. (f) XPS valence band spectrum of α-MnO_2. g) Photocurrent of α-MnO_2/rGO photocathodes in ZIBs under alternatively illumination. h) Schematic mechanism of photoassisted-ZIBs based on α-MnO_2/rGO electrodes during photocharge.

electron-hole separation capability of α-MnO_2/rGO photoelectrodes, with the photoresponse current of ≈2 μA.

Figure 2 depicts the electrochemical properties of the α-MnO_2-based PRZIBs. To exclude the photothermal effect, rate performances were measured under dark, thermal (coin cells without the optical window under 1 sun), and light conditions (coin cells with the optical window under 1 sun). As illustrated in Figure 2a, α-MnO_2 ZIBs exhibited similar rate performance under thermal and dark conditions, confirming the negligible influence of photothermal effects. Notably, the photo-assisted α-MnO_2 ZIBs demonstrated significantly improved specific capacities across all current densities (from 0.2 A g^{-1} to 2 A g^{-1}). The capacity returned to 356.4 mAh g^{-1} at 0.2 A g^{-1} with a recovery rate of 115.7%, indicating excellent rate performance under illumination. The galvanostatic charge/discharge curves (GCD) profiles at 0.2 A g^{-1} (Figure 2b) reveal charge/discharge capacities of 343.2/308.1 mAh g^{-1} under illumination, compared to only 213.9/207.2 mAh g^{-1} in dark conditions. Additionally, two characteristic discharge plateaus at 1.43 V and 1.32 V were observed in both conditions, corresponding to H^+ and Zn^{2+} intercalation, respectively.[18] Importantly, illumination reduced the polarization potential (ΔE) between the charge and discharge plateaus ($\Delta E_{illumination}$ = 0.24 V and ΔE_{dark} = 0.27 V), as well as reduced the discharge plateau. Also, the voltage changes of α-MnO_2 PRZIBs before and after illumination are provided in Figure S4 (Supporting Information) (current density: 0.2 A g^{-1}). Upon switching to light, the voltage was increased during discharge and decreased during charge, demonstrating that light can mitigate the polarization. Similar trends were observed at higher current densities (Figure S5a–e, Supporting Information), with irradiation consistently reducing the polarization voltages and prolonging the discharging plateaus. It should be pointed out that the relatively low coulombic efficiency in Figure 2b stemmed from the photo-induced proton transfer causing corrosion in the anode (Zn foil),[17b] which diminishes at high current density (Figure S5c–e, Supporting Information). We also investigated the GCD profiles at different current densities under light (Figure 2c) and dark (Figure S5f, Supporting Information) conditions, and the corresponding photo-assisted capacities (Figure S6, Supporting Information) as well. Interestingly, even at the high current density (2 A g^{-1}), the photo-assisted ZIBs demonstrated specific charge/discharge capacity enhancement of 83.1%/83.2%. This suggests that photoenergy overcomes the kinetic limitations of α-MnO_2 and ions/protons by supplying additional charge carriers to participate in the electrochemical reaction.[13] In addition, the fitted Nyquist curves from electrochemical impedance spectroscopy (EIS) measurements of α-MnO_2 ZIBs reveal a 62.8% reduction in charge transfer resistance (R_{ct}) under illumination (180.1 Ω versus 481.4 Ω in dark conditions).

The galvanostatic intermittent titration technique (GITT) analysis (Figure S7, Supporting Information) further confirms accelerated ionic diffusion under illumination, with a photo-promoted diffusion coefficient ($D_{Zn^{2+}}$) 5–10 times higher than that under dark conditions. These results verify that the photogenerated carriers, which can be efficiently separated by α-MnO_2/rGO photoelectrodes, significantly contribute to charge transfer and ionic diffusion in bulk electrodes. Moreover, the capacity retention of photo-assisted α-MnO_2 ZIBs was investigated (Figure 2e). The cyclic stability tests revealed that photo-assisted batteries maintained 208.1 mAh g^{-1} capacity at the current density of 0.5 A g^{-1}, whereas the dark-cycled counterparts maintained only 133.5 mAh g^{-1} after the 150th cycle (Figure S8, Supporting Information). These results are consistent with the aforementioned rate performances and also demonstrate the excellent cycling stability of photo-assisted α-MnO_2 ZIBs. Figure 2f–h systematically show the photo-charging abilities of the α-MnO_2 ZIBs without an external electric power supply. Since the potential continues to rise slowly during the static rest period after the discharge process (self-charge, blue curve in Figure 2f),[13] it is necessary to exclude the contribution of this part when evaluating the

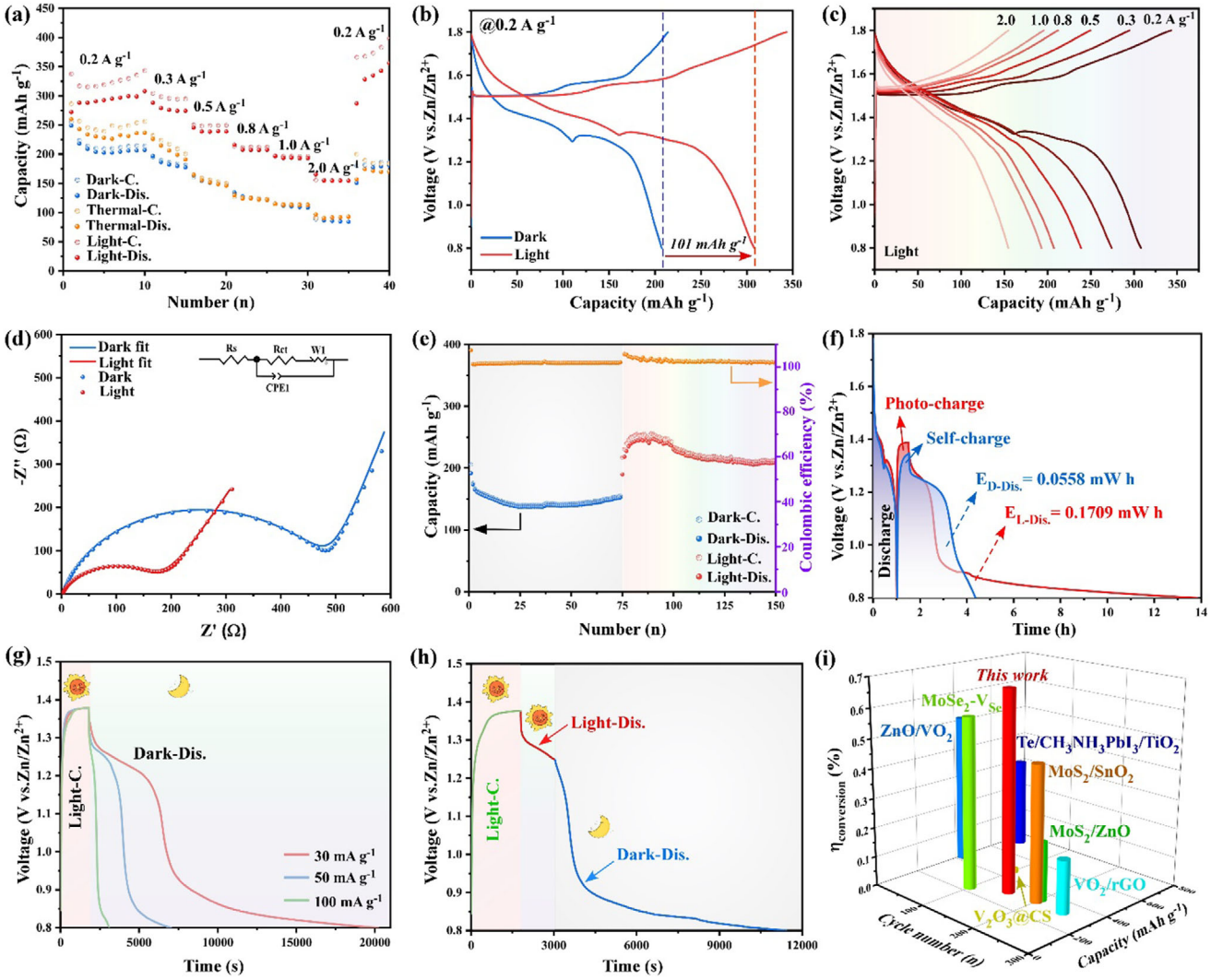

Figure 2. Electrochemical properties of photo-rechargeable α-MnO_2 ZIBs. a) Rate performances of α-MnO_2 ZIBs in dark, thermal, and light conditions. b) Galvanostatic charge and discharge (GCD) curves for α-MnO_2 ZIBs in dark and under illumination at 0.2 A g^{-1}. c) GCD curves for α-MnO_2 ZIBs at current densities from 0.2 A g^{-1} to 2 A g^{-1} in light conditions. d) EIS plots for α-MnO_2 ZIBs in dark and light conditions. e) Cyclic curves for α-MnO_2 ZIBs switching between in dark and light conditions at 0.5 A g^{-1}. f) Light-charge and dark-discharge for α-MnO_2 ZIBs at 20 mA g^{-1}. g) Light-charge and dark-discharge for α-MnO_2 ZIBs at 20 mA g^{-1}, 50 mA g^{-1}, and 100 mA g^{-1}. h) Light-charge, light-discharge, and dark-discharge for α-MnO_2 ZIBs at 50 mA g^{-1} to mimic all-day application. i) Comparison of the performances with other PRZIBs and this work in recent years.

conversion efficiency for photo-rechargeable ZIBs (PRZIB). So, following complete discharge under dark conditions, the batteries underwent sequential photo-charging and self-charging (as shown in Figure 2f), after which their discharge performance was evaluated at a current density of 20 mA g^{-1}. Here, the discharge capacities of photo-charged and self-charged ZIBs were found 0.1709 mW h and 0.0558 mW h, respectively. Therefore, solar-electric conversion efficiency ($\eta_{conversion}$) in the α-MnO_2 PRZIB can be calculated by Equation (1).

$$\eta_{conversion} = \frac{E_{output}}{E_{input}} 100\% = \frac{E_{L-discharge} - E_{D-discharge}}{(P_{in} \times A \times t)} 100\% \quad (1)$$

where, $E_{L-discharge}$ refers to the photo-charged discharge capacity in mW h, $E_{D-discharge}$ refers to the self-charged discharge capacity in mW h, P_{in} is the power density of incident light in mW cm^{-2}, A is the irradiated area in cm^2, and t is the photo-charging time in hours, respectively. We estimated the conversion efficiency to be 0.46% using this equation. However, in most previous literature reports, the solar energy conversion efficiency was calculated without subtracting the self-charging energy (Table S1, Supporting Information), which corresponds to 0.68% in this work. This demonstrates a superior conversion ability compared to most recently reported PRZIBs (Figure 2i). Figure 2g represents the discharge profiles at various specific currents (30, 50, and 100 mA g^{-1}) after 0.5 h of photo-charging. It can be observed that the open circuit voltage (V_{OC}) of the PRZIB reached to 1.39 V after photo-charging. Furthermore, Figure 2h illustrates the photo-charging abilities of α-MnO_2 PRZIBs under simulated diurnal operating

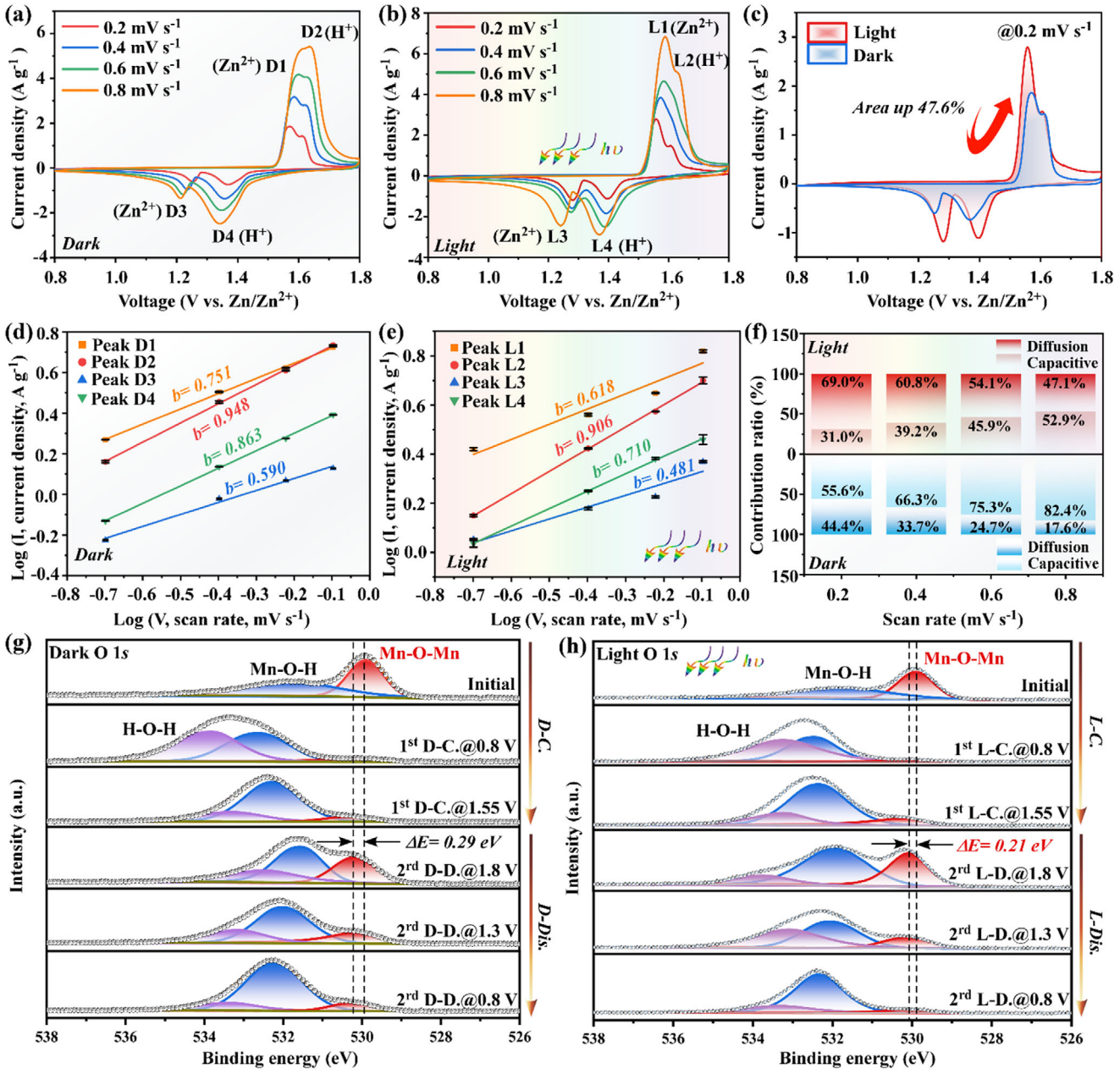

Figure 3. Electrochemical and ex situ XPS characterizations of α-MnO_2/rGO photoelectrodes. a,b) CV curves of ZIBs based on α-MnO_2/rGO photoelectrodes at scan rates of 0.2-0.8 mV s^{-1} under dark (a) and illumination (b). c) Comparison of CV curves of ZIBs based on α-MnO_2/rGO photoelectrodes under dark and illumination at 0.2 mV s^{-1}. d,e) Corresponding b-values under dark and illumination of (a) and (b). f) Capacitance contributions at different scan rates under dark and illumination derived from (d) and (e). g,h) ex situ XPS characterizations of O 1s spectra for α-MnO_2 during charge/discharge process under dark and illumination.

conditions, highlighting their potential for practical all-day application.[17a]

To comprehensively study the photo-promoted electrochemical reaction kinetics in α-MnO_2 PRZIBs, we performed CV tests at various scan rates under both dark and light conditions. **Figure** 3a,b present the CV curves obtained between 0.8 and 1.8 V vs. Zn/Zn^{2+} over a range of scan rates from 0.2 to 0.8 mV s^{-1}. Two pairs of typical anodic/cathodic peaks are observed under both dark and light conditions. The cathodic peaks at 1.33-1.37 V (Peak 4) and 1.20-1.25 V (Peak 3) are attributed to Zn^{2+}/H^+ intercalation, respectively. Meanwhile, the anodic peaks at 1.55-1.65 V (Peak 1 and 2) indicated Zn^{2+}/H^+ deintercalation.[18] Notably, the CV curves obtained under illumination exhibited significantly sharper peaks and higher current densities compared to those measured in dark conditions, indicating the enhanced kinetics for both Zn^{2+}/H^+ intercalation and deintercalation processes. Figure 3c shows a comparison of CV curves under dark and light conditions at 0.2 mV s^{-1}, where significant shifts in

the redox peak positions are observed. Specifically, Peak 4 (H^+ intercalation) shifts from 1.37 V (dark) to 1.40 V (illumination), as well as Peak 3 (Zn^{2+} intercalation) shifts from 1.25 V (dark) to 1.28 V (illumination). The anodic peaks (Peak 2 and Peak 1) also shift to lower potential (both peaks with $\Delta E = 0.01$ V). These changes indicate a significant reduction in the polarization of the redox reaction under illumination, which also suggests that photo energy enhances the electrochemical reaction activity and accelerates the electrode kinetics.[13,20] Additionally, the quantitative analysis shows a 47.6% increase in the integrated area of CV curves under illumination, revealing enhanced charge storage capacity. Consistent behavior was observed across higher scan rates (0.4 mV s^{-1}, 0.6 mV s^{-1}, and 0.8 mV s^{-1}, Figure S9, Supporting Information). Moreover, Figure 3d,e provides the ***b*** values calculated form the CV curves in Figure 3a,b to investigate the origin of capacity improvement under illumination. For both conditions, the ***b*** values were always less than 1, indicating that charge storage contributions arise from both capacitive and diffusion-controlled processes.[21] However, as shown in Figure S10 (Supporting Information), for the photo-assisted ZIBs, the ***b*** values decreased at different scan rates compared to dark conditions, suggesting that the photo energy significantly facilitated ion diffusion behavior.[17b] Specifically, based on Figure S11 (Supporting Information), the pseudocapacitive behavior and ion diffusion can be proportionally investigated by the following equation:

$$i = k_1 v + k_2 v^{1/2} \quad (2)$$

where i denotes the peak current, $k_1 v$ and $k_2 v^{1/2}$ represent the capacitive and ionic diffusion contribution, respectively.[21] As shown in Figure 3f and Figures S12 and S13 (Supporting Information), the proportion of ion diffusion increased from 44.4%, 33.7%, 24.7%, and 17.6% (dark conditions) to 69.0%, 60.8%, 54.1%, and 47.1% (light conditions) at scan rates of 0.2 mV s^{-1}, 0.4 mV s^{-1}, 0.6 mV s^{-1}, and 0.8 mV s^{-1}, respectively. This demonstrates that ion diffusion always contributes more on capacity under illumination, i.e., photo energy acts as a driving force for ion diffusion. Furthermore, it is important to emphasize that the improved capacity contribution form the ion diffusion does not compromise the pseudocapacitive behavior of the system.[17b]

To further determine the extent of Zn^{2+}/H^+ intercalation/deintercalation during charge/discharge process, we performed ex situ XPS characterization on α-MnO_2 based ZIBs under both dark and light conditions. The deconvoluted O 1*s* spectra (Figure 3g,h) reveal three distinct peaks at 529.8 eV, 531.5 eV, and 532.5 eV, corresponding to Mn-O-Mn, Mn-O-H, and H-O-H, respectively.[21] The quantitative analysis of the Mn-O-Mn peak area (details available in Table S2, Supporting Information) demonstrated markedly different behavior under illumination. During the first cycle of charging (0.8 V→1.55 V→1.8 V), the proportion of Mn-O-Mn peaks increased from 5.4% to 28.2% under dark conditions, while it significantly increased from 2.1% to 30.4% under illumination. Oppositely, during the subsequent discharge process (1.8 V→1.3 V→0.8 V), the proportion of Mn-O-Mn decreased from 28.2% to 9.5% under dark conditions, while it dramatically decreased from 30.4% to 5.9% under light. These results confirm enhanced ions (Zn^{2+}/H^+) intercalation/deintercalation into the α-MnO_2. Consequently, both pseudocapacitive and ion diffusion behaviors were promoted under light conditions, but the enhancement of ion diffusion behavior was more significant.

In addition, H-O-H peaks in O 1*s* spectra are closely related to the Zn-derived intermediate products, i.e. $Zn_4SO_4(OH)_6$, while Mn-O-H peaks are associated with H^+ insertion of α-MnO_2.[22] Therefore, variations in both H-O-H and Mn-O-H peaks can be taken as the reflection of H^+ intercalation. Specifically, the proportion of H-O-H and Mn-O-H peaks reached 94.1% under illumination versus 90.5% in dark condition during the second discharge, indicating photo-promoted H^+ intercalation. This is consistent with the previously reported photo-enhanced proton transfer in ZIBs,[17b] which creates an alkaline environment on the cathode surface favoring the formation of $Zn_4SO_4(OH)_6$. Notably, for the photo-assisted ZIBs, illumination reduced the binding energy shifts of Mn-O-H (Table S3, Supporting Information) and Mn-O-Mn ($\Delta E_{light} = 0.21$ eV versus $\Delta E_{dark} = 0.29$ eV), indicating a photo-inhibited Jahn-Teller effect in α-MnO_2 cathodes. This can be related to the formation of stronger hydrogen bonds (H•••O) due to the positive charge of H^+ and the strong interaction of O^{2-} in the α-MnO_2 insertion layer under light conditions, thereby weakening the change in Mn-O bonds.[22b] Also, the H-O-H (Table S4, Supporting Information) peaks exhibited a higher upshift (533.6 eV) for photo-assisted ZIBs after charging, suggesting strengthened hydrogen bonds (H•••O) in the α-MnO_2 framework. From another perspective, this photo-promoted H^+ intercalation enhanced hydrogen bonding between α-MnO_2 and intercalated H^+, which effectively constrained the stretching of [MnO_6] octahedra along the z-axis and mitigated irreversible Mn^{2+} dissolution.[21,22b]

The complementary ex situ XPS spectra of Mn 2*p* (Figure S14, Supporting Information) demonstrate prominent shifts of Mn $2p_{3/2}$ peaks toward higher binding energies after charging and the opposite shifts after discharging, indicating the reversible Mn^{2+}/Mn^{4+} redox behavior during cycling.[23] Notably, the observed binding energy shifts were attenuated under illumination. This also indicates the passivation of α-MnO_2 dissolution under illumination. The ICP-OES results of Mn/Zn elemental ratio after cycles also confirm the suppressed dissolution of Mn^{2+} under illumination (Figure S15, Supporting Information). To further demonstrate the photo-induced suppression of Jahn-Teller distortion in MnO_2, we performed ex situ Raman spectroscopic analysis (Figure S16, Supporting Information). Three characteristic peaks of MnO_2 were observed—V_1 bonds (640-680 cm^{-1}, symmetric Mn-O stretching), V_2 bonds (572-589 cm^{-1}), and V_3 bonds (500-515 cm^{-1}), Mn-O stretching in [MnO_6] octahedra.[24] Under dark conditions, substantial V_1 peak shifts during the charge and discharge process (Figure S13a, Supporting Information) indicate the irreversible changes in [MnO_6] local octahedron coordination. This reflects a severe structural change in the [MnO_6] octahedron due to the Jahn-Teller distortion in dark. In contrast, the illuminated samples (Figure S13b, Supporting Information) maintain nearly constant V_1 peak positions during cycles, indicating effective suppression of Jahn-Teller distortion.

To investigate the time-resolved Zn^{2+}/H^+ co-intercalation kinetics of photo-assisted α-MnO_2 ZIBs, we performed in situ XRD characterizations under both dark and light conditions (Figure S17, Supporting Information). **Figure 4a,c** present the GCD profiles at 0.1 A g^{-1} alongside the corresponding 2D

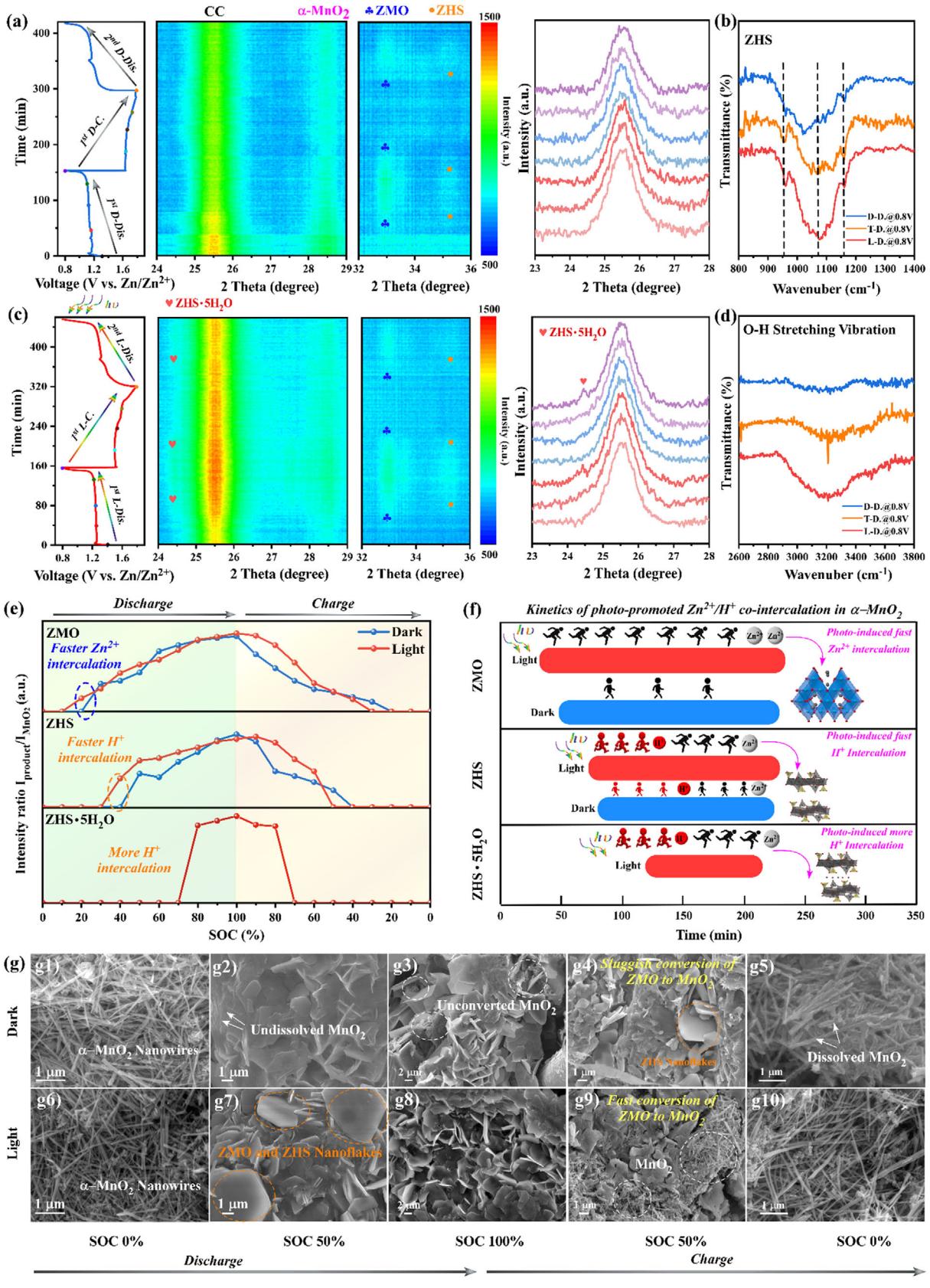

contours and 1D pattern of in situ XRD spectra of α-MnO_2 ZIBs under dark (Figure 4a) and light conditions (Figure 4c) in the first discharge (1st Dis. red in 1D pattern), the first charge (1st C. blue in 1D pattern) and the second discharge (2nd Dis. purple in 1D pattern) process, respectively. Initially, both cathodes exhibited three characteristic peaks at 25.52°, 28.58°, and 37.54°, corresponding to the peaks of carbon cloth (CC), α-MnO_2 (3 1 0), and α-MnO_2 (2 1 1), respectively. During discharge, a new characteristic peak of $ZnMn_2O_4$ (ZMO) gradually emerged at 32.89° under both dark and light conditions, indicating Zn^{2+} intercalation. As discharge progressed, an additional peak of $Zn_4SO_4(OH)_6{\cdot}H_2O$ (ZHS) appeared at 35.18°, resulting from the alkaline environment near the cathode surface caused by H^+ intercalation.[25] The charging process demonstrated sequential disappearance of ZHS followed by the ZMO peaks. During the second discharging, the peaks of ZMO and ZHS reappeared, confirming the reversible co-intercalation/deintercalation of Zn^{2+}/H^+ under both dark and light conditions. Notably, for the α-MnO_2 PRZIBs (Figure 4c), a distinct peak gradually developed at 24.39° with the continuation of discharging, which corresponds to the formation of $Zn_4SO_4(OH)_6{\cdot}5H_2O$ (ZHS·$5H_2O$).[26] This new intermediate product clearly indicates a larger amount of H^+ intercalation into α-MnO_2 due to the photo-promoted proton transfer under illumination.

Further, to observe the photothermal effects on the formation of ZHS·$5H_2O$, we analyzed the FT-IR spectra of electrodes discharged to 0.8 V (cutoff voltage) under dark, thermal, and light conditions (Figure 4b, d). While the ZHS characteristic peaks (at 960 cm^{-1}, 1070 cm^{-1}, and 1160 cm^{-1})[27] appear in all cases, their intensities are strongest under illumination. It suggests the formation of more ZHS under light compared to the dark conditions. Furthermore, the O-H bond vibrations (2600 cm^{-1}−3800 cm^{-1}) prove that ZHS formed under illumination contains abundant water (ZHS·$5H_2O$), while no significant O-H peak intensity can be observed under dark and thermal conditions. Meanwhile, Figure S18 (Supporting Information) shows the ex-situ XRD spectra of electrodes under dark, thermal, and light conditions, where the cathodes were taken out to remove the residual electrolyte on surface at different SOC. Here, the minimal formation MnOOH (21.52°)[28] in dark/thermal conditions compared to illuminated samples provide direct evidence for photo-promoted H^+ insertion to form excess MnOOH (Figure S18c, Supporting Information). So, the local thermal effect can be excluded.

Figure 4e systematically summarizes the peak intensity changes of different intermediate products (ZMO, ZHS, and ZHS·$5H_2O$) during the charge/discharge cycles under dark and light conditions. The characteristic peaks intensities of the intermediate products are normalized to the peak intensity of α-MnO_2 in initial cathodes. Under illumination, ZMO and ZHS formation initiates at earlier state of charge (20% and 40% SOC, respectively), and disappear at 30% SOC and 50% SOC, respectively. Under dark conditions, ZMO and ZHS formation initiates at 30% SOC and 50% SOC, while disappear at 20% SOC and 40% SOC, respectively. These results indicate accelerated co-intercalation/deintercalation of Zn^{2+}/H^+ in α-MnO_2 under illumination. To better visualize the kinetics of Zn^{2+}/H^+ co-intercalation/deintercalation under both dark and light conditions, Figure 4f provides a Gantt chart of the different intermediate products, i.e. ZMO, ZHS and ZHS·$5H_2O$, during charge/discharge process under dark and light conditions. Since the charge/discharge experiments were conducted at identical current density, the duration of the intermediate products reflects the extent of the electrochemical reaction in the α-MnO_2 cathodes. Overall, all the intermediate products exist for a longer duration under light conditions than under dark conditions, indicating that the redox reaction of α-MnO_2 is more complete under light conditions. This prolonged reaction window leads to an enhanced capacity of the photo-assisted batteries.

To further verify the conversion process of α-MnO_2 at cathodes, we performed ex situ SEM analysis of the cathodes at different SOC under both dark and light conditions (Figure 4g). With both conditions exhibit the intercalation/deintercalation dominant reaction mechanisms, significant morphological changes emerged. During discharge to 50% SOC, the dark conditions preserved abundant unconverted α-MnO_2 nanowires on the cathode surface (Figure 4g2), whereas illumination promoted the formation of large hexagonal nanosheets (ZHS or ZHS·$5H_2O$ nanosheets)[29] on the cathode surface at the same stage (Figure 4g7), indicating the photo-promoted discharge reaction kinetics. Complete discharge to 100% SOC under dark conditions left some undissolved α-MnO_2 nanowires (Figure 4g3) on the cathode surface, while the cathode surface was found almost completely covered by large hexagonal nanosheets under light conditions (Figure 4g8). This suggests that the discharge reaction is more complete under illumination. Subsequently, when charging to 50% SOC, α-MnO_2 nanowires reappeared more efficiently on the cathode surface under illumination compared to the dark conditions (Figure 4g4,4g9). At 100% SOC, some crosslinked nanosheet-structured Zn-vernadites [19] were observed on the α-MnO_2 nanowires under dark conditions (Figure 4g5), while α-MnO_2 nanowires with clear edges were noticed under light conditions (Figure 4g10). These morphological observations demonstrate that the intercalation/deintercalation reaction proceed more completely under illumination.

Meanwhile, the cross-sectional SEM images of the electrodes discharged to 0.8 V under dark and light conditions (Figure S19, Supporting Information) indicate that the SEI layers formed under illumination were thicker than that in dark, attributable to the formation of additional ZHS and ZHS·$5H_2O$. These findings are also consistent with the ex situ XPS results, where the attenuated intensity variation of Mn-O-Mn peaks during

Figure 4. Time-resolved characterizations of the intermediate products in photo-assisted α-MnO_2 ZIBs. a,c) The GCD curves at 0.1 A g^{-1} and the corresponding 2D contours and 1D pattern of in situ XRD spectra of α-MnO_2 ZIBs under dark (a) and light conditions (c) in the first discharge (1st Dis. red in 1D pattern), the first charge (1st C. blue in 1D pattern) and the second discharge (2nd Dis. purple in 1D pattern) process. b,d) The FT-IR spectra of the electrodes discharged to a cutoff voltage of 0.8 V are obtained under dark, thermal, and light conditions. e) Trend plots of discharge products at different state of charge (SOC). f) Gantt chart of different discharge products under dark and light conditions. g) Ex situ SEM images of the α-MnO_2 cathodes at different SOC under dark and light conditions.

discharge under illumination indicates enhanced intercalation of H^+ kinetics. Based on these characterizations, we can conclude that photoenergy promotes the kinetics of Zn^{2+}/H^+ co-intercalation/deintercalation in α-MnO_2 ZIBs, especially facilitating the insertion of H^+. It results in the formation of a large number of ZHS and ZHS·$5H_2O$ as the "protective layers" to suppress the dissolution of α-MnO_2.[30] As a result, the strengthened hydrogen bonding in α-MnO_2 weakens the Jahn-Teller distortion, leading to improved capacity and cycling performance in the photo-assisted α-MnO_2 ZIBs.

To further investigate the underlying mechanism of the photo-promoted Zn^{2+}/H^+ co-intercalation in α-MnO_2 ZIBs, we performed in situ FT-IR tests to observe the regulation of H-bonds and solvation structure of Zn^{2+} in aqueous electrolyte (2 M $ZnSO_4$ with 0.2 M $MnSO_4$) under dark and light conditions (details in Figure S20, Supporting Information). Figure 5a,c present the GCD profiles at 0.2 A g^{-1} alongside the corresponding 2D contours of in situ FT-IR patterns for α-MnO_2 ZIBs under dark and light conditions, respectively, with detailed spectra at different SOCs shown in Figure 5b,d. Three characteristic vibrational modes were observed under both conditions (dark and light) located at 1095 cm^{-1} (SO_4^{2-} stretching), 1210 cm^{-1} (Mn^{2+} coordination), and 2750–3750 cm^{-1} (stretching vibration of O-H).[31] Besides, the original FT-IR spectra of 2 M $ZnSO_4$ and 2 M $ZnSO_4$+0.2 M $MnSO_4$ electrolytes are shown in Figure S21 (Supporting Information). Compared with pure $ZnSO_4$ electrolyte, $ZnSO_4$+$MnSO_4$ electrolyte shows a characteristic peak at 1210 cm^{-1}, which refers to Mn^{2+}. The peak intensity of SO_4^{2-} attenuated during discharge, which reveals the continuous consumption of SO_4^{2-} in ZHS formation. Conversely, the release of SO_4^{2-} into the electrolyte during the charge process was reflected by the gradual increase of corresponding peak intensity. Notably, under illumination the SO_4^{2-} peak intensity was continually enhanced during the first discharge cycle, which should be attributed to the thermal effect on the electrolyte caused by irradiation during the in situ FT-IR test. To further verify our hypothesis, we conducted in situ FT-IR tests of Zn | Zn symmetry batteries with 2 M $ZnSO_4$+0.2 M $MnSO_4$ electrolyte under illumination, as shown in Figure S22 (Supporting Information). Here, the peak intensity of SO_4^{2-} remained unchanged after the discharge process in 1st cycle. Thus, it can be affirmed that the evaporation of electrolyte gets saturation after the 1st discharge under light conditions, and the result is independent of photothermal effect. Additionally, the normalized intensity changes (ΔA_i, i = SO_4^{2-} or Mn^{2+}) of SO_4^{2-} and Mn^{2+} under dark and light conditions were calculated by Equation 3 to show the variation in ionic concentration (Figure 5e).

$$\Delta A_i = A_{t,i} - A_{0,i} \tag{3}$$

where $A_{t,i}$ refers to the peak intensity of SO_4^{2-} or Mn^{2+} at different SOC and $A_{0,i}$ refers to the peak intensity of SO_4^{2-} or Mn^{2+} during the 1st cycle of discharge.

The larger intensity variations of SO_4^{2-} under illumination (versus dark conditions) indicate the involvement of more SO_4^{2-} ions in the formation of ZHS. This finding is consistent with the results demonstrated by in situ XRD. Moreover, the intensity of Mn^{2+} remained unchanged under illumination throughout the cycles, while it was increased under dark conditions after cycling. Since the extra Mn^{2+} can only come from the cathodes, this clearly indicates that the dissolution of α-MnO_2 is suppressed by the "protective layers" under light conditions. Also, the digital images of dissembled cathode shells in Figure S23 (Supporting Information) directly show the formation of fewer Mn^{2+}-based products under light. In addition, the Mn^{2+} peak position exhibits a blue-shift under illumination (1280 cm^{-1}) compared to the dark conditions (1210 cm^{-1}). This shift is attributed to the weakened solvation of Mn^{2+} by H_2O and the stronger electrostatic attraction between Mn^{2+} and SO_4^{2-} under illumination.[32] Additionally, the illumination induced a slight red-shift in the O-H stretching vibration, which arises from the strengthened H-bonding interactions (Figure 5f,g), These stronger H-bonds drive water molecules to associate into larger cluster structures, thereby reducing the frequency of O-H stretching vibrations. As a result, the desolvation of hydrated Zn^{2+} ions, i.e. $Zn(H_2O)_x^{2+}$ becomes more favorable under illuminated conditions.

To better characterize the illumination-induced changes in solvation chemistry, particularly the dynamic structure of H-bonds in the bulk electrolyte, we analyzed different types of O-H bonds based on the proton donor (H atom as ***D***)-acceptor (O atom as ***A***) mechanism at initial, fully discharged, and fully charged states.[31a] Previous studies on the local H-bonds in $ZnSO_4$ electrolyte have demonstrated that solute salts can induce diverse local interactions between H_2O and anions/cations, altering the H_2O solvation clusters to form both Zn^{2+}-bound and Zn^{2+}-free H_2O molecules (Figure S24, Supporting Information). As shown in Figure 5e,f, there are mainly five types in the O-H stretching vibration modes for Zn^{2+}-free H_2O: DAA, DDAA, DA, DDA, and free-OH (ordered by increasing wavenumber). Among these types, DAA and DDAA are considered as "strong hydrogen bonds" (S-H), while DA, DDA, and free-OH refer to "weak hydrogen bonds" (W-H). Here, we statistically summarized the proportion of S-H and W-H at different charge/discharge stages under dark (Figure 5f) and light conditions (Figure 5g). Under dark conditions, the proportion of S-H and W-H remains unchanged. However, under illumination, the proportion of S-H gradually increased from 55.64% to 62.31% during the charge/discharge process, while the proportion of W-H decreased correspondingly. In contrast, no obvious changes were observed in the proportion of S-H under dark conditions (52.29% to 52.09%). This notable increase in the proportion of S-H indicates that photoenergy effectively enhances the interaction of H_2O, thereby reducing the presence of free H_2O molecules in the electrolyte and reducing the number of bound H_2O in the Zn^{2+} solvated structure. According to the pioneering research on the relation between H-bonds evolution and Zn^{2+} solvation/desolvation, this stronger interaction of H_2O in the bulk electrolyte facilitates the replacement of H_2O molecules in the solvation shell of Zn^{2+}, forming the typical $[Zn\text{-}(H_2O)_x(SO_4)_y]^{2-2y}$ solvation structure. Furthermore, the strengthened interaction between SO_4^{2-} and Zn^{2+} under illumination promotes Zn^{2+} desolvation in the bulk electrolyte, ultimately enhancing the specific capacity.[33] Additionally, from the perspective of desolvation energy, the binding energy (ΔE) variation in different $Zn(H_2O)_x^{2+}$ (x = 6 to 1) clusters is generally from 0.17 eV to 1.19 eV ($\Delta E_{max} = \Delta E_{Zn(H_2O)_2^{2+}} - \Delta E_{Zn(H_2O)^{2+}}$), which

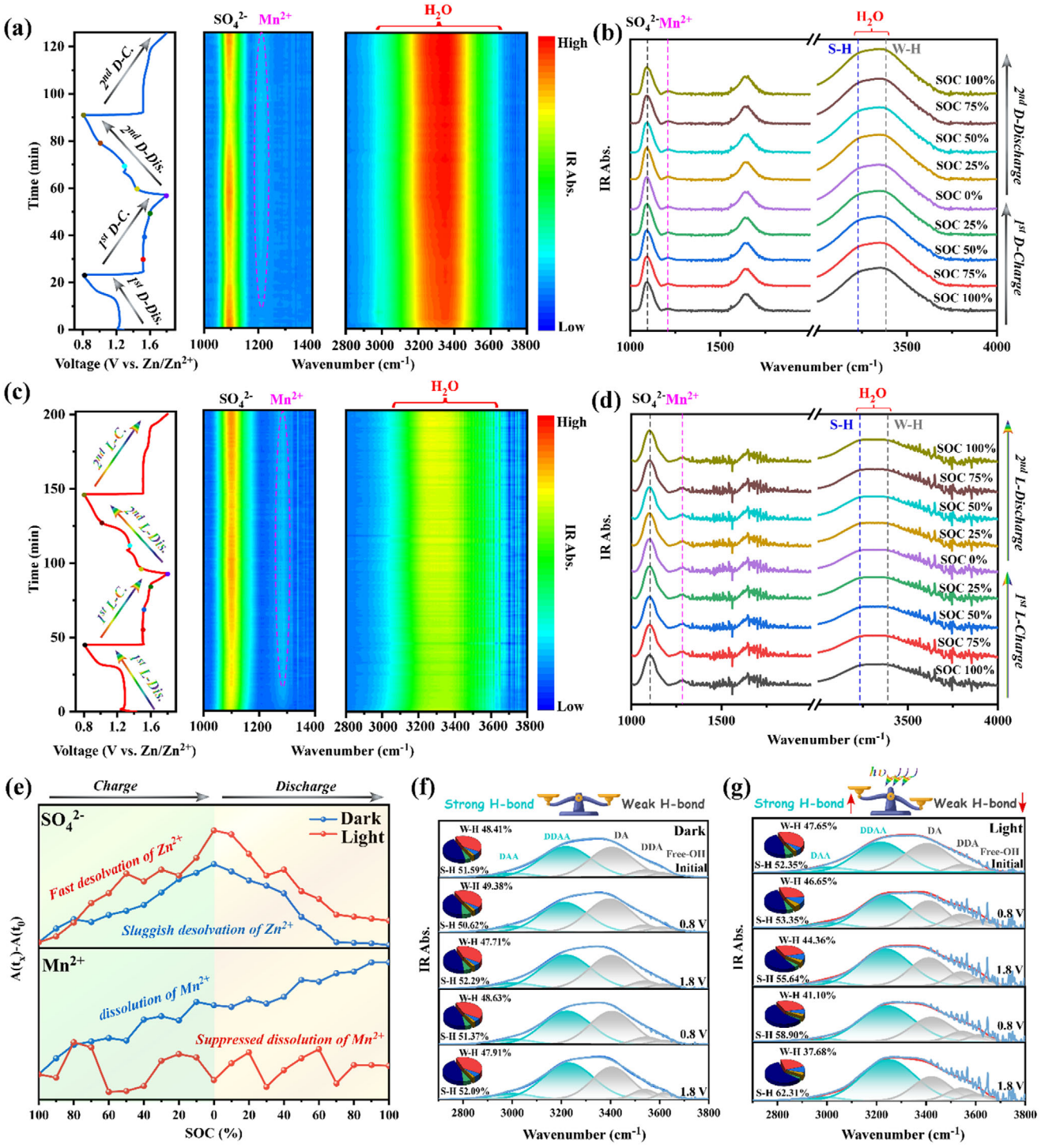

Figure 5. In situ FT-IR characterizations for dark and photo-assisted α-MnO_2 ZIBs. a,c) The GCD curves and corresponding 2D contours of in situ FT-IR patterns under (a) dark and (c) light conditions, respectively. b,d) FT-IR spectra at different SOCs in the 1st cycle of charging and the 2nd cycle of discharging under (b) dark and (d) light conditions, respectively. e) Trends of intensity changes of SO_4^{2-} and Mn^{2+} under dark and light conditions extracted from (b) and (d). f,g) Hydrogen bonding changes, including the changes of strong and weak H-bonds, under dark and light conditions.

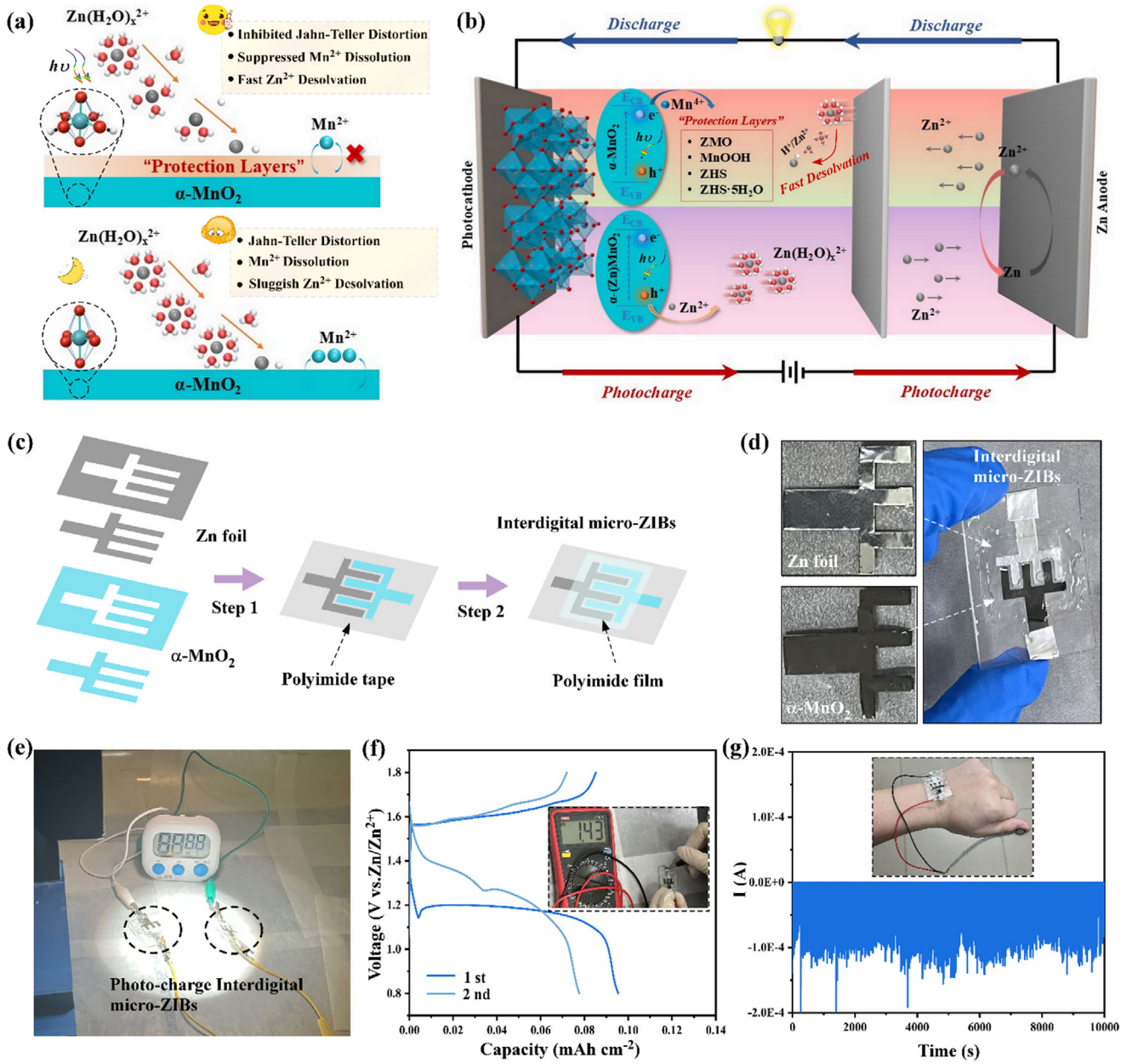

Figure 6. Mechanism and applications of α-MnO_2 based PRZIBs. a) The promoted effects of photoenergy on α-MnO_2 based photoelectrodes. b) Reaction of photo-generated carriers in α-MnO_2 based PRZIBs during photocharge and discharge process. c) Schematic diagram of the fabrication process of interdigital α-MnO_2 based micro-PRZIBs. d) Digital graphs of Zn anode, α-MnO_2 cathode and interdigital α-MnO_2 based micro-PRZIBs. e) Digital graphs of the timer powered by a pair of α-MnO_2 based micro-PRZIBs. f) GCD curves of α-MnO_2 based micro-PRZIBs at 0.1 mA cm^{-2}. g) The i-t curves of pressure sensor powered by a single microdevice after photo-charge.

also can be fully overcome by the photoenergy of 1 sun (1.65 eV≈3.1 eV).[34]

To eliminate the influence of OH^- concentration changes on O-H stretching vibration caused by ZHS formation, we conducted in situ FT-IR measurements using Zn | Zn symmetric batteries with identical electrolyte under illumination, which yielded a similar result as shown in Figure S22 (Supporting Information). Additionally, we note that potential electrolyte evaporation due to the thermal effects may lead to variations in concentration and consequently affect the O-H vibrations. To evaluate this concentration effect, we collected and analyzed the remaining electrolyte after the in situ FT-IR test with Zn | Zn symmetric batteries (Figure S25, Supporting Information). The proportion of S-H in the symmetric batteries was 53.01%, significantly lower than that under light conditions (62.37%). This demonstrates that the thermal evaporation has minimal effect on O-H stretching vibrations in the electrolyte during illumination. Based on these comprehensive analyses of H-bond dynamics, we conclude that photoenergy directly enhances H_2O molecule interactions in the bulk electrolyte by reducing the proportion of free water

content, thereby accelerating Zn^{2+} desolvation kinetics during discharge.

Based on the aforementioned in situ measurements and analyses, the photocharging mechanism of α-MnO_2 based PRZIBs can be summarized as **Figure** 6a,b. Overall, the photo-promoted effects in α-MnO_2 based PRZIBs can be manifested through three key aspects– *(1) Inhibited Jahn-Teller Distortion*: the photo-promoted proton transfer and H^+ intercalation in α-MnO_2 strengthen hydrogen bonding within the structure, thereby stabilizing Mn-O bond stretching along the z-axis in the MnO_6 octahedra. *(2) Suppressed Mn^{2+} Dissolution*: the rapid Zn^{2+}/H^+ co-intercalation facilitates the conversion of intermediate products, i.e. ZHS, ZHS·5H_2O, ZMO, etc., which act as "protective layers" to Mn^{2+} dissolution. (3) Accelerated Zn^{2+} Desolvation in the electrolyte: the abundant photogenerated holes in α-MnO_2 during discharge accelerates the reaction $h^+ + Zn - MnO_2 \rightarrow Zn^{2+} + MnO_2$. This process enhances Zn^{2+} desolvation in the electrolyte, while directly overcomes the high desolvation energy barrier can be by irradiation. In summary, the electrochemical reactions in α-MnO_2 based PRZIBs can be summarized as follows.

$$Cathode: \ (Zn)\ MnO_2 \rightarrow e^- + h^+ \tag{4}$$

$$MnO_2 + H^+ + e^- \leftrightarrow MnOOH \tag{5}$$

$$4Zn^{2+} + SO_4^{2-} + 6OH^- + nH_2O \leftrightarrow Zn_4SO_4(OH)_6 \cdot nH_2O \tag{6}$$

$$MnO_2 + Zn^{2+} + 2e^- \leftrightarrow ZnMn_2O_4 \tag{7}$$

$$Anode: \ Zn - 2e^- \leftrightarrow Zn^{2+} \tag{8}$$

To advance the practical application of α-MnO_2-based PRZIB in wearable micro-devices, we fabricated interdigital α-MnO_2-based micro-PRZIBs. Figure 6c,d schematically illustrates the fabrication process along with a digital photograph of the completed micro-PRZIBs (see details in Methods). The device consists of α-MnO_2 cathode and Zn anode adhered to a polyimide strip and assembled into flexible interdigital micro-ZIBs. Impressively, after being totally discharged, two digital micro-ZIBs can power a timer solely through photocharging, without any requiring external power supply (Figure 6e). Figure 6f presents the GCD profiles of a single α-MnO_2 based micro-PRZIB, demonstrating an area specific capacity of 0.1 mAh cm^{-2} at a current density of 0.1 mA cm^{-2}. Furthermore, as shown in Figure 6g, a single α-MnO_2 based micro-PRZIBs can provide sufficient energy to operate a pressure sensor for continuously capturing changes within 10 000 s after photocharging. These results highlight the outstanding potential applications of α-MnO_2 based micro-PRZIBs as miniaturized energy conversion-storage devices for future wearable technologies, i.e., wearable electronic devices and smart textiles.

3. Conclusions

In summary, this work reports a photo-rechargeable ZIB system with high solar energy conversion efficiency based on the photoactive α-MnO_2 cathodes. Significant research efforts, including the in situ XRD and FT-IR studies, have been dedicated to reveal the underlying mechanism in photo-promoted electrochemical reactions for the first time. Compared to previous studies, this work systematically explains the advantages of intrinsic light effects on PRZIBs. Thanks to the excellent visible light absorption and efficient electron/hole separation capability of photoactive α-MnO_2 cathodes, which synergistically promoted the Zn^{2+}/H^+ co-intercalation and Zn^{2+} desolvation processes at the cathode-electrolyte interface. Consequently, the α-MnO_2 based PRZIBs achieved excellent rate performance with high discharge capacity (308.1 mAh g^{-1}), and the light conversion efficiency of 0.68%. Furthermore, practical applications of the α-MnO_2 based interdigital micro-PRZIBs on timer and pressure sensor demonstrated their promising future for self-powered wearable electronics. This study provides crucial insights into the mechanism of aqueous PRZIBs and offers design principles for integrated energy conversion-storage systems.

Supporting Information

Supporting Information is available from the Wiley Online Library or from the author.

Acknowledgements

Z.Z. and C.D. contributed equally to this work. This work was financially supported by the National Key Research and Development Program of China (2023YFB3809301, 2022YFE0114800) and the National Natural Science Foundation of China (No. 62474127, 52472245). Authors greatly thank Prof. Liqiang Mai in Wuhan University of Technology for his carefully discussion and financial support on this work.

Conflict of Interest

The authors declare no conflict of interest.

Data Availability Statement

The data that support the findings of this study are available from the corresponding author upon reasonable request.

Keywords

α-MnO2, H+/Zn2+ co-intercalation, in-situ study, photo-rechargeable batteries, zinc-ion batteries

Received: January 3, 2025
Revised: April 21, 2025
Published online:

[1] a) M. Yang, D. Wang, Y. Ling, X. Guo, W. Chen, *Adv. Funct. Mater.* **2024**, *34*, 2410398; b) E. Aydin, T. G. Allen, M. De Bastiani, A. Razzaq, L. Xu, E. Ugur, J. Liu, S. De Wolf, *Science* **2024**, *383*, adh3849; c) S. H. Reddy, F. Di Giacomo, A. Di Carlo, *Adv. Energy Mater.* **2022**, *12*, 2103534.
[2] a) H. Tang, Y. Bai, H. Zhao, X. Qin, Z. Hu, C. Zhou, F. Huang, Y. Cao, *Adv. Mater.* **2024**, *36*, 2212236; b) J. Lv, J. Xie, A. G. A. Mohamed, X. Zhang, Y. Wang, *Chem. Soc. Rev.* **2022**, *51*, 1511.

[3] R. Roy, R. Greeshma, A. Basith, R. Banerjee, A. K. Singh, *Energy Storage Mater.* **2024**, *71*, 103680.
[4] A. S. Mary, G. Mahendra, R. Roy, M. K. Ganesha, A. K. Singh, *EES Batteries* **2025**, *1*, 23.
[5] a) C. Li, S. Cong, Z. Tian, Y. Song, L. Yu, C. Lu, Y. Shao, J. Li, G. Zou, M. H. Rümmeli, *Nano Energy* **2019**, *60*, 247; b) Y.-H. Liu, J. Qu, W. Chang, C.-Y. Yang, H.-J. Liu, X.-Z. Zhai, Y. Kang, Y.-G. Guo, Z.-Z. Yu, *Energy Storage Mater.* **2022**, *50*, 334; c) B. D. Boruah, A. Mathieson, B. Wen, C. Jo, F. Deschler, M. De Volder, *Nano Lett.* **2020**, *20*, 5967.
[6] a) Q. Zeng, Y. Lai, L. Jiang, F. Liu, X. Hao, L. Wang, M. A. Green, *Adv. Energy Mater.* **2020**, *10*, 1903930; b) J. Pan, K. Yuan, X. Mi, Y. Lu, Y. Yu, J. Yang, S. Dou, P. Qin, *ACS Nano* **2023**, *17*, 21360; c) H. Liu, X. Gao, Y. Lou, H. K. Liu, S. X. Dou, Z. Bai, N. Wang, *Adv. Energy Mater.* **2024**, *14*, 2402381.
[7] M. Yu, X. Ren, L. Ma, Y. Wu, *Nat. Commun.* **2014**, *5*, 5111.
[8] R. Wang, H. Liu, Y. Zhang, K. Sun, W. Bao, *Small* **2022**, *18*, 2203014.
[9] S. Ahmad, C. George, D. J. Beesley, J. J. Baumberg, M. De Volder, *Nano Lett.* **2018**, *18*, 1856.
[10] X. Y. Du, L. N. Song, S. Liang, Y. F. Wang, Y. Wang, H. F. Wang, J. J. Xu, *Angew. Chem., Int. Ed.* **2024**, *63*, 202411845.
[11] R. Roy, G. Mahendra, A. K. Singh, *Chem. Eng. J.* **2024**, *500*, 156870.
[12] L. Jiao, X. Zhang, Y. Feng, J. Lin, D. Yuan, Y. Wang, *Angew. Chem., Int. Ed.* **2023**, *62*, 202306506.
[13] T. Yang, H. Mao, Q. Zhang, C. Xu, Q. Gao, X. Cai, S. Zhang, Y. Fang, X. Zhou, F. Peng, S. Yang, *Angew. Chem., Int. Ed.* **2024**, *63*, 202403022.
[14] X. Zhang, W.-L. Song, M. Wang, J. Tu, H. Jiao, S. Jiao, *Energy Storage Mater.* **2022**, *45*, 586.
[15] W. Wang, C. Li, S. Liu, J. Zhang, D. Zhang, J. Du, Q. Zhang, Y. Yao, *Adv. Energy Mater.* **2023**, *13*, 2300250.
[16] X. Gao, D. Tian, Z. Shi, N. Zhang, R. Sun, J. Liu, H. S. Tsai, X. Xiang, W. Feng, *Small* **2024**, *20*, 2405627.
[17] a) B. D. Boruah, A. Mathieson, B. Wen, S. Feldmann, W. M. Dose, M. De Volder, *Energy Environ. Sci.* **2020**, *13*, 2414; b) W. Zha, Q. Ruan, L. Ma, M. Liu, H. Lin, L. Sun, Z. Sun, L. Tao, *Angew. Chem., Int. Ed.* **2024**, *63*, 202400621; c) Y. Zhao, T. He, J. Li, C. Zhu, Y. Tan, K. Zhu, S. Chou, Y. Chen, *Angew. Chem., Int. Ed.* **2024**, *63*, 202408218.
[18] Q. Li, C. Wang, Y. Zhu, W. Du, W. Liu, M. Yao, Y. Wang, Y. Qian, S. Feng, *Chem. Eng. J.* **2024**, *485*, 150077.
[19] S. Cui, D. Zhang, G. Zhang, Y. Gan, *J. Mater. Chem. A* **2022**, *10*, 25620.
[20] H. Liu, P. Wu, R. Wang, H. Meng, Y. Zhang, W. Bao, J. Li, *ACS Nano* **2023**, *17*, 1560.
[21] Z. Xu, J. Wang, W. Zhang, Z. Shi, Y. Feng, C. Liu, H. Fu, Z. Yong, Q. Li, *J. Mater. Chem. A* **2024**, *12*, 25491.
[22] a) Y. Wang, Y. Zhang, G. Gao, Y. Fan, R. Wang, J. Feng, L. Yang, A. Meng, J. Zhao, Z. Li, *Nano-Micro Lett.* **2023**, *15*, 219; b) S. Wang, Z. Yuan, X. Zhang, S. Bi, Z. Zhou, J. Tian, Q. Zhang, Z. Niu, *Angew. Chem., Int. Ed.* **2021**, *60*, 7056.
[23] X. Li, Y. Sun, L. Zhou, H. Wang, B. Xie, W. Lu, J. Ning, Y. Hu, *Mater. Horiz* **2024**, *11*, 4133.
[24] J. Liang, Y. Zhao, L. Ren, M. Li, Q. Zhang, Y. Wang, X. Sun, M. Chuai, X. Wang, W. Liu, *Adv. Funct. Mater.* **2025**, 2501135.
[25] Y. Ren, S. Zhang, B. Yin, J. R. Loh, Y. Ding, X. Huang, J. Li, H. Li, T. Ma, *Batteries Supercaps* **2023**, *6*, 202300132.
[26] Q. Chen, X. Lou, Y. Yuan, K. You, C. Li, C. Jiang, Y. Zeng, S. Zhou, J. Zhang, G. Hou, J. Lu, Y. Tang, *Adv. Mater.* **2023**, *35*, 2306294.
[27] L. Godeffroy, I. Aguilar, J. Médard, D. Larcher, J. M. Tarascon, F. Kanoufi, *Adv. Energy Mater.* **2022**, *12*, 2200722.
[28] Q. Zhang, J. Zhao, X. Chen, R. Yang, T. Ying, C. Cheng, B. Liu, J. Fan, S. Li, Z. Zeng, *Adv. Funct. Mater.* **2024**, *34*, 2306652.
[29] Z. Wang, Y. Fang, J. Shi, Z. Ma, X. Qu, P. Li, *Adv. Energy Mater.* **2024**, *14*, 2303739.
[30] X. Guo, J. Zhou, C. Bai, X. Li, G. Fang, S. Liang, *Mater. Today Energy* **2020**, *16*, 100396.
[31] a) X. Yu, M. Chen, Z. Li, X. Tan, H. Zhang, J. Wang, Y. Tang, J. Xu, W. Yin, Y. Yang, D. Chao, F. Wang, Y. Zou, G. Feng, Y. Qiao, H. Zhou, S.-G. Sun, *J. Am. Chem. Soc.* **2024**, *146*, 17103; b) R. Jiang, T. Naren, Y. Chen, Z. Chen, C. Zhang, Y. Xie, L. Chen, Y. Qi, Q. Meng, W. Wei, L. Zhou, *Adv. Funct. Mater.* **2024**, *34*, 2411477.
[32] T. Wu, C. Hu, Q. Zhang, Z. Yang, G. Jin, Y. Li, Y. Tang, H. Li, H. Wang, *Adv. Funct. Mater.* **2024**, *34*, 2315716.
[33] W. Xu, J. Li, X. Liao, L. Zhang, X. Zhang, C. Liu, K. Amine, K. Zhao, J. Lu, *J. Am. Chem. Soc.* **2023**, *145*, 22456.
[34] C. Dai, B. Liu, *Energy Environ. Sci.* **2020**, *13*, 24.